Chemical Physics Letters 622 (2015) 9–14

Contents lists available at ScienceDirect

Chemical Physics Letters

journal homepage: www.elsevier.com/locate/cplett

A large red-shift in the photoluminescence emission of $Mg_{1-x}Sr_xTiO_3$

Mayumi M. Nakata[a], Tatiana M. Mazzo[b], Graziela P. Casali[a], Felipe A. La Porta[a,c,*], Elson Longo[c]

[a] INCTMN, LIEC, Departamento de Química, Universidade Federal de São Carlos, P.O. Box 676, 13565-905 São Carlos, SP, Brazil
[b] Universidade Federal de São Paulo, Av. Alm. Saldanha da Gama, 89 – Ponta da Praia – Santos/SP – CEP: 11030-400, 13565-905, SP, Brazil
[c] INCTMN, LIEC, Instituto de Química, Universidade Estadual Paulista, P.O. Box 355, 14800-900 Araraquara, SP, Brazil

ARTICLE INFO

Article history:
Received 24 September 2014
In final form 7 January 2015
Available online 14 January 2015

ABSTRACT

In this letter, we report a detailed study of the influence of the synthesis and the optical properties of Sr-doped $MgTO_3$ powders synthesized via a polymeric precursor method. Our findings explain the shift in PL behavior from blue to near-infrared (NIR) emission, which is caused by different concentrations of deep and shallow defects in the samples and thus enables the design of differently colored materials. Additionally, the present results provide useful insights into designing a new series of NIR-emitting materials that have potential applications in emerging technologies ranging from optoelectronics to the biomedical field.

1. Introduction

Perovskite oxides are a fascinating class of multifunctional inorganic materials that have attracted much attention in recent years [1–6]. Perovskite structures have the general formula ABO_3, where the divalent metal (A) is a network modifier and tetravalent metal sites (B) are network formers for these structures [2]. The Perovskite material ABO_3 structure can adopt five phases, cubic, tetragonal, orthorhombic, trigonal, and monoclinic polymorphs depending on the tilting and rotation of the $[BO_6]$ polyhedral clusters in the lattice [3]. In this context, considerable effort has been devoted to the production of perovskite oxide materials with a large variety of morphologies and sizes, due to their high potential for use in light-emitting diodes, photocatalysts, sensors, microwave dielectrics, and photovoltaic applications [4–7]. Understanding the relationship between the structural and electronic order-disorder effects in the crystalline materials is crucial in designing novel materials with tunable physical and chemical properties [8,9].

Among oxide perovskites, magnesium titanate $MgTiO_3$ (MTO) is an important semiconductor material characterized by an ilmenite structure with space group R-3H and a rhombohedral crystal phase which has received much attention in recent years, due to the unique properties of MTO. This material shows utility for a wide range of applications in electronic systems such as capacitors and mobile communications as well as radar and satellite broadcasting [7,10–12]. The size, shape and synthetic environment are crucial factors in determining the chemical and physical properties of MTO materials [7]. A large number of synthetic strategies have been developed for the growth of these materials, such as solid-state reaction [10], thermal decomposition of peroxide precursors [11], hydrothermal processing [12]. However, the problems that persist in the preparation of MTO for these synthesis routes are, in particular, the presence of Mg_2TiO_4 and $MgTi_2O_5$ phases and a relatively high sintering temperature (>1400 °C) required to obtain the pure phase. The polymeric precursor method is a very versatile method of synthesis due to the use of low temperature heat treatments, which reduces segregated phases, leading to a better distribution of cations in the polymer resin and complete chemical homogeneity on a molecular scale in the system [13]. The method of synthesis involved in preparing these materials influences the structural defects, which are responsible for modifying the properties of these systems.

A considerable effort has been made recently to understand the intrinsic and visible emissions in MTO [7,14,15], and this knowledge plays a key role in streamlining the physical properties of the system. In particular, the photoluminescence (PL) properties are an important quantum optical phenomenon and are one of the most powerful methods for studying the order-disorder effects in semiconductors [8,9]. The doping process in semiconductors often causes significant alterations in the structural and electronic properties of these materials, and is the most promising strategy

* Corresponding author at: INCTMN, LIEC, Departamento de Química, Universidade Federal de São Carlos, P.O. Box 676, 13565-905 São Carlos, SP, Brazil.
E-mail address: felipe_laporta@yahoo.com.br (F.A. La Porta).

http://dx.doi.org/10.1016/j.cplett.2015.01.011
0009-2614/

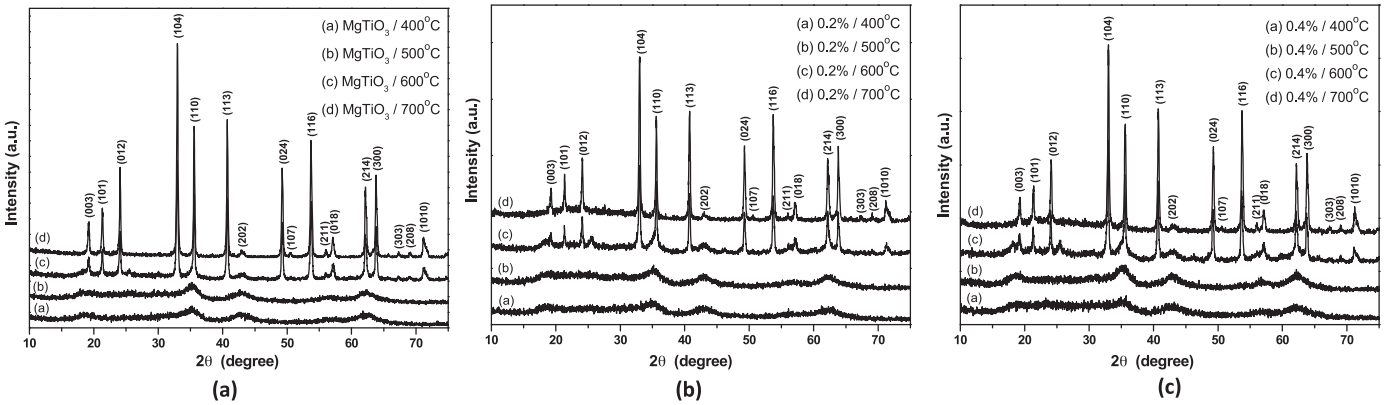

Figure 1. XRD patterns of the synthesized MTO and MTO:Sr calcined at various temperatures for 2 h: (A) 0.0, (B) 0.2 and (C) 0.4% of Sr^{+2}-doped MTO.

to further enhance their properties and applications in materials science [5,6,15–17]. However, few studies have been reported on near-infrared (NIR) emissions for such particles [14].

Here we report the development of a series of novel $Mg_{1-x}Sr_xTiO_3$ (MTO:Sr) materials with intense PL emissions at room temperature in the NIR region. Non-doped and MTO:Sr materials were successfully synthesized via the polymeric precursor method. The obtained materials were analyzed by X-ray diffraction (XRD), micro-Raman (MR) spectroscopy, field emission scanning electron microscopy (FE-SEM), ultraviolet–visible (UV–vis) and photoluminescence (PL) measurements. In this context, our objective is focused primarily on analyzing the structural, morphological and optical properties of this novel MTO:Sr material as a function of the annealing temperature and different Sr^{+2}-doped concentrations.

2. Experimental details

MTO and MTO:Sr materials were successfully synthesized via a polymeric precursor method. All materials were used without further purification or treatment. Magnesium acetate $(CH_3CO_2)_2Mg$ (98%, Aldrich), titanium butoxide $Ti[O(CH_2)_3CH_3]_4$ (99%, Aldrich), $Sr(NO_3)_2$ (99.93%, Aldrich), ethylene glycol, $C_2H_6O_2$ (99.5%, Synth), and citric acid $C_6H_8O_7$ (99.5%, Synth) were used as raw materials. In a typical procedure, titanium citrate was formed by dissolution of titanium butoxide in an aqueous solution of citric acid under constant stirring. The citrate solution was stirred at 90 °C to obtain a clear homogeneous solution. $(CH_3CO_2)_2Mg$ was added in a stoichiometric quantity to the Ti citrate solution. After the homogenization of the Mg^{2+} cations, $C_2H_6O_2$ was added to promote a polyesterification reaction. For the preparation of the MTO:Sr powers, different molar concentrations of $Sr(NO_3)_2$ were added to the solution in a stoichiometric quantity relative to the Mg^{2+} and Ti citrate concentrations. The citric acid/ethylene glycol ratio was fixed at 60/40 by mass. These powders were heat treated initially at 350 °C for 2 h using a 5 °C min^{-1} constant heating rate, and they were then annealed at 400, 500, 600 and 700 °C in a tubular furnace with a gradient control for 2 h in an oxygen atmosphere.

The obtained powders were structurally characterized by XRD using a Rigaku-DMax/2500PC with Cu Kα radiation (λ = 1.5406 Å) in the 2θ range from 10° to 75° with 0.02° min^{-1} increments. MR measurements were performed using a T64000 spectrometer (Jobin-Yvon, France) triple monochromator coupled to a CCD detector. Spectra were obtained using the 514.5 nm wavelength of an argon ion laser; its maximum output power was maintained at 8 mW. The morphologies of the MTO and MTO:Sr powders were observed by FE-SEM using an FEG-VP JEOL, and are presented in the Supporting Information. The optical properties were analyzed by

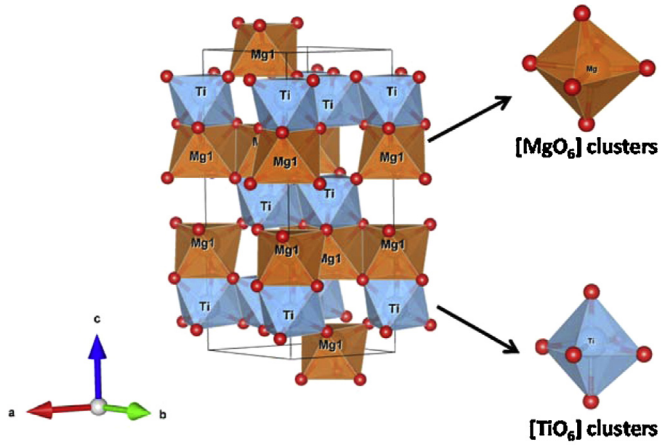

Figure 2. Structure of the rhombohedral MTO compound and illustrations of the octahedral $[MgO_6]$ and $[TiO_6]$ clusters.

means of UV–vis absorption spectra and PL measurements. UV–vis spectra were taken using a Cary 5G spectrophotometer (Varian, USA) in diffuse reflection mode. PL spectra were collected with a Thermal Jarrel-Ash Monospec monochromator and a Hamamatsu R446 Photomultiplier. The 350.7 nm (2.57 eV) exciting wavelength of a krypton ion laser (Coherent Innova) was used with the output of the laser maintained at 200 mW. All measurements were performed at room temperature.

3. Results and discussion

The XRD patterns were performed on the MTO and MTO:Sr samples to provide long-range structural information and to investigate the purity and polycrystalline nature of these materials. Figure 1 shows the XRD pattern obtained for the MTO and MTO:Sr samples heat treated from 400° to 700 °C. On the basis of these results, the structural transformation as a function of the heat treatment can be monitored. The results shows that the samples heat treated at 400 °C and 500 °C are amorphous, i.e. are completely disordered at long-range. The beginning of the crystallization of the MTO phase can be observed at 600 °C, where the appearance of diffraction peaks indicates that above this temperature the samples have a higher crystallinity with a greater long-range order (see Figure 1). However, it is still possible to observe the formation of a second phase $MgTi_2O_5$ at this given temperature. In the pure phase MTO powders are obtained at 700 °C and all of the diffraction peaks can be indexed as a rhombohedral ilmenite-type structure with space group R-3H (see Figure 2), which is in agreement with the

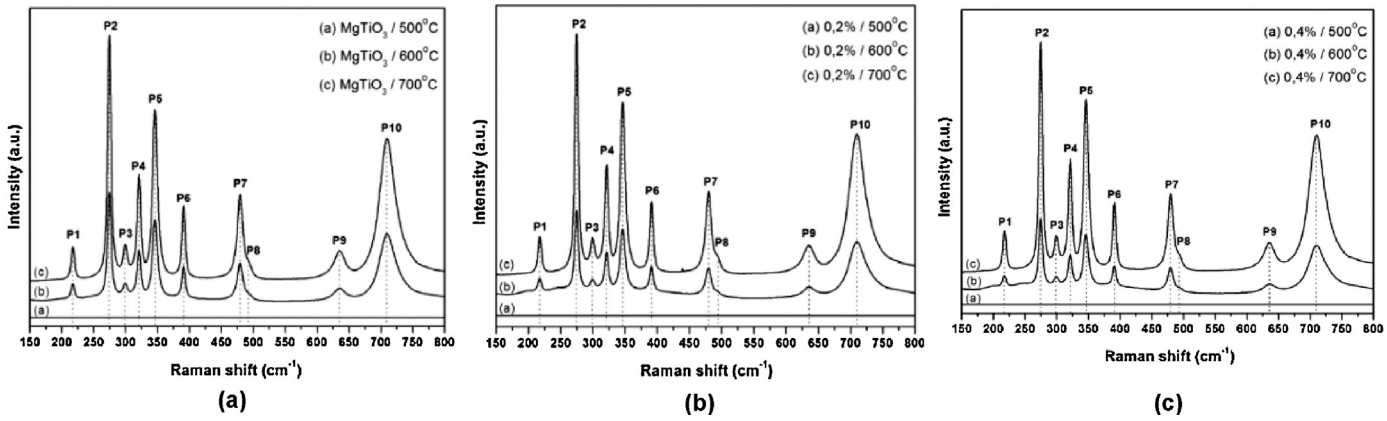

Figure 3. Micro-Raman spectra of the synthesized MTO and MTO:Sr calcined at various temperatures for 2 h: (a) 0, (b) 0.2 and (c) 0.4% of Sr^{+2}-doped MTO.

respective Joint Committee on Powder Diffraction Standards (JCPDS) card 06-0494 and with the diffraction peaks previously reported in the literature [18–20].

Figure 2 shows a representation of the unit cells of the MTO rhombohedral ilmenite-type structure with space group R-3H. The Visualization for Electronic and Structural Analysis (VESTA) program (version 3.1.8 for Windows) [21] was used for the construction of the MTO structure model. In Figure 2, the MTO belongs to the ilmenite-type structure based on a rhombohedral close packing array of oxide ions where Mg^{2+} and Ti^{+4} ions occupy the octahedral clusters [MgO_6] and [TiO_6], respectively.

To gain insight into the structure of the MTO and MTO:Sr samples at short-range, MR spectroscopy was employed. Figure 3 shows the MR spectrum of the MTO and MTO:Sr for powders heat treated from 400° to 700 °C. No Raman active modes of MTO samples heat treated at 400 °C and 500 °C, regardless of doping, are observed, indicating that these samples are Raman inactive and are completely disordered in the short-range. These results are in agreement with the XRD (see Figure 1), and we conclude the structural organization at the long-range and short-range of the MTO phase begins at 600 °C. The group theory for MTO in the rhombohedral structure [22–24] predicts the crystals should have 10 distinct vibrational Raman-active modes ($5A_G + 5B_G$), which are observed for the samples heat treated at 600 °C and 700 °C (see Figure 3). All Raman-active modes can be observed for the samples treated at temperatures of 600 °C and 700 °C, which confirms that the MTO and MTO:Sr samples are structurally ordered at the short-range. In other words, increasing the annealing temperature favors the structural organization of the MTO and MTO:Sr samples at the short-range.

Table 1 lists the ten positions (P1-P10) of the Raman modes for all samples. These results show a red-shift in the Raman spectra and are attributed to different distortions and bond lengths of the [MgO_6] and [TiO_6] clusters. The Ag modes situated at 217 and 299 cm^{-1} arise from the vibrations of Mg and Ti atoms along the *z*-axis. On the other hand, the other Ag modes observed at 391, 493 and 710 cm^{-1} are ascribed to the vibrations of O atoms and the intense E_g mode at 275 cm^{-1} is related to the anti-symmetric breathing vibration of the O octahedron. In particular, for the modes at 493 and 710 cm^{-1} the six O atoms show breathing-like vibrations, each with a different vibration direction into the octahedral configuration.

Based on our results reported in Table 1, the Eg modes located at 321 cm^{-1} and 346 cm^{-1} can be described as the twisting of the O octahedron with the vibrations of Mg and Ti atoms parallel to the *xy*-plane. The Eg modes located at 480 and 635 cm^{-1} are due to the anti-symmetric breathing and twisting vibrations of the O octahedra with the cationic vibrations parallel to the *xy*-plane [7,24]. Another important aspect concerns the Eg modes at 480 cm^{-1} where both Mg and Ti atoms are involved in the vibration, whereas the mode at 635 cm^{-1} is associated to the Ti—O stretch [24]. Our results show a greater variation in the Raman-active vibrational modes of the [TiO_6] clusters in the rhombohedral structure of the MTO and MTO:Sr for powders heat treated from 400° to 700 °C (see Table 1). In particular, the experimental Raman spectra for MTO in the rhombohedral structure previously reported by other authors [7,22–24] is in good agreement with this study.

The optical properties of the MTO and MTO:Sr were analyzed by means of UV–vis absorption spectra and PL measurements. In general, the optical band gap energies are controlled by the degree of structural and electronic disorder in the lattice which enable a change in the optical transitions offering an opportunity for tuning their properties by band gap engineering. In this context, a semi-empirical relationship was used to calculate the optical experimental band gap energy (E_{gap}) using the following Eq. (1):

$$\alpha h\nu = C_1(h\nu - E_{gap})^n, \quad (1)$$

Table 1
Raman peak positions observed in the MR spectra (in cm^{-1}) of the synthesized MTO and MTO:Sr calcined at 700 °C for 2 h.

	MTO_{Powder} [20]	MTO_{Powder} [22]	$MTO_{Thin\ Films}$ [7]	MTO	MTO:Sr 0.2%	MTO:Sr 0.4%
Ag	229	225	228	217	218	218
Eg	285.8	281	285	275	275	275
Ag	310	306	311	299	299	299
Eg	330.9	328	332	321	320	320
Eg	356.5	353	358	346	346	346
Ag	400.2	398	401	391	390	390
Eg	488.9	486	491	480	480	480
Ag	501.2	500	501	493	493	493
Eg	643.9	641	643	635	636	636
Ag	716.4	715	717	710	710	710

Table 2
Optical band gap energy values obtained for the samples (in eV).

Temperature	400 (°C)	500 (°C)	600 (°C)	700 (°C)
MTO	3.5	3.5	3.8	4.0
0.2%	3.6	3.6	3.6	4.0
0.4%	3.6	3.6	3.7	4.0

where α is the linear absorption coefficient of the material, $h\nu$ is the photon energy, C_1 is a proportionality constant, E_{gap} is the optical band gap and n is a constant associated with different types of electronic transitions ($n = 1/2$, 2, 3/2 or 3 for direct allowed, indirect allowed, direct forbidden and indirect forbidden transitions, respectively); for more details on this methodology see reference [9]. In particular, the E_{gap} values obtained for the samples are in good agreement with those of MTO reported in the literature (3.72–3.19 eV) [14] and by theoretical calculations (5.46 eV) [7]. Based on the results reported in Table 2, an increase is observed in the value of the optical band gap due to the increase of the heat treatment temperature, which indicates a reduction in the defect concentration observed for crystalline materials or an ordered structure which is in good agreement with our results of the XRD patterns and MR spectra.

Figure 4 shows the PL spectra at room temperature of the synthesized MTO and MTO:Sr heat treated at various temperatures for 2 h. According to different temperatures and doping concentrations of Sr^{+2}, the PL behavior of MTO causes a visible red-shift suggesting a change in the local chemical environment and disorder in the crystalline systems of the MTO microcrystals which enables the design of different colored material for PL emissions and requires that certain localized states should exist in the forbidden band gap, which were observed in the UV–vis measurements. Figure 4(a, b) illustrates the PL behavior for samples heat treated at 400° and 500 °C and confirms a broad band covering the visible electromagnetic spectrum in the range from 400 to 800 nm, with maximum emission at 550 nm to 715 nm, respectively, when excited by a 350.7 nm laser. In this case, the PL behavior for the MTO and MTO:Sr is typical of the multiphonon process, i.e., a system where relaxation occurs by several paths involving the participation of numerous states within the band gap of the material [25,26]. A major change in the PL behavior can be observed with the increase in crystallinity of the samples calcined at 600° and 700 °C, as shown in Figure 4(c, d), when compared to the samples obtained at the lower calcination temperatures (see Figure 4(a, b)). In particular, the PL emissions in the visible region are completely suppressed and intense emission in the NIR region can be observed as a large red-shift in the PL behavior as shown in Figure 4(c, d).

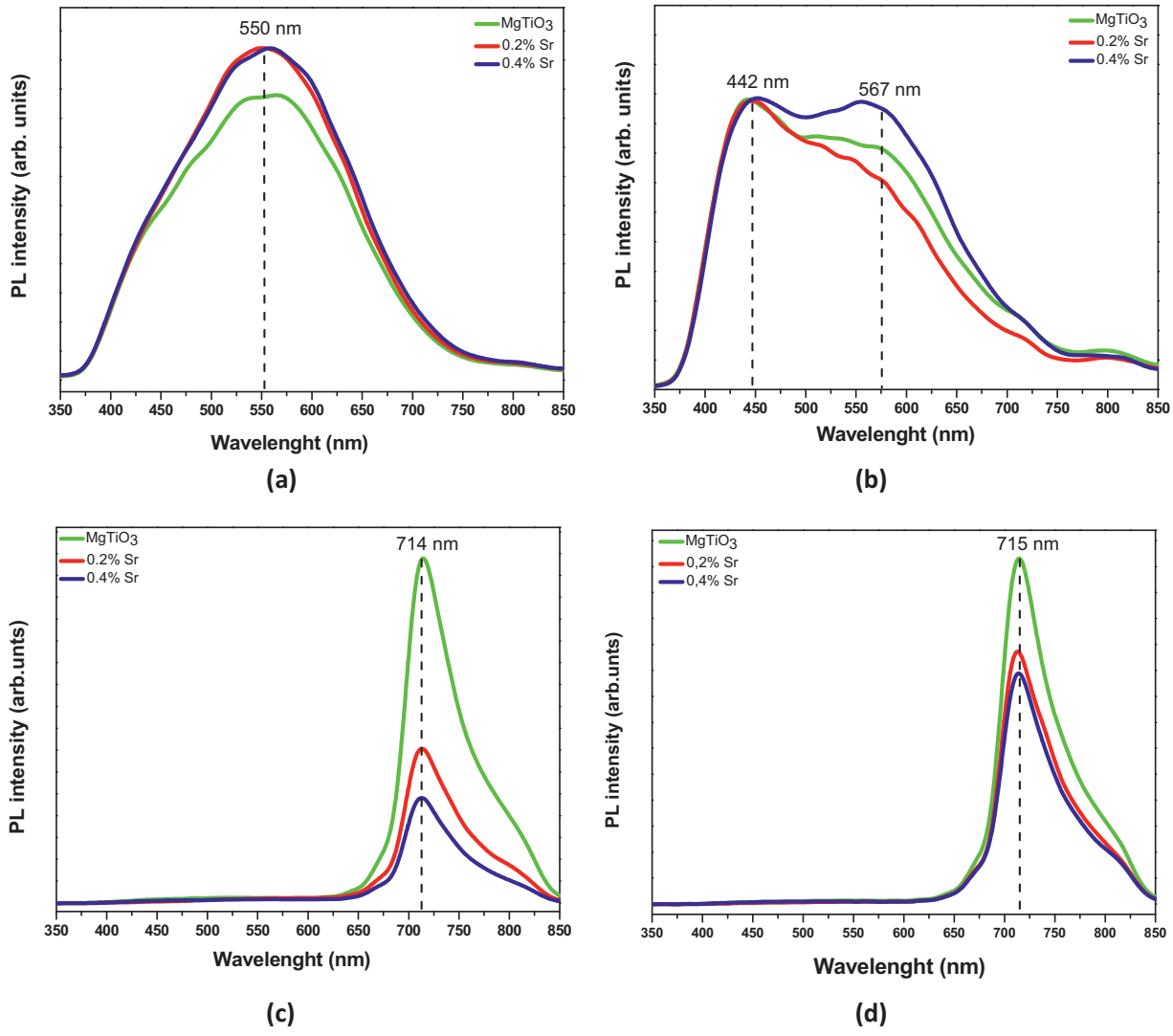

Figure 4. PL spectra at room temperature of the synthesized MTO and MTO:Sr calcined at various temperatures for 2 h: (a) 400, (b) 500, (c) 600 and (d) 700 °C.

Structural and electronic order-disorder effects in semiconductor materials have a major influence on the optical properties [7–9,25,26]. PL is an interesting technique for probing certain structural aspects to provide information at the short- and medium-range, where the degree of the local order is such that structurally inequitable sites can be distinguished by their different types of electronic transitions and are linked to a specific structural arrangement [26,27]. In this context, Longo and co-workers offered an explanation based on the Kröger–Vink notation to explain the vacancy formation in perovskite oxide materials [25]. The local structure and the disorder in the crystalline structure as well as the variation in the interface/bulk-surface might be responsible for the different PL behaviors of the MTO and MTO:Sr materials, which can be easily visualized in Figure 4.

In this case, we offer a possible explanation for the observed changes in the PL behavior of these materials in terms of the structural and electronic order-disorder effects leading to the formation of complex clusters. The increase in the band gap is due to the reduction of intermediary levels at the short-range and long-range, which are associated with a larger organization of network modifiers due to the increase of the concentration of Sr-doped MTO, and resulting in a shift from blue to red PL emissions for the synthesized MTO and MTO:Sr calcined at various temperatures for 2 h. The effects can be represented by complex clusters as follows: $[TiO_6]_o^x$ and $[MgO_6]_o^x$ clusters and $[TiO_5 \cdot V_O^x]_d$ and $[MgO_5 \cdot V_O^x]_d$ clusters (where o = order and d = disorder), using Kröger–Vink notation to characterize the local chemical environment and disorder in crystalline materials. In particular, oxygen vacancy can occur in three different charge states (where $V_O^Z = V_O^X, V_O^\bullet, V_O^{\bullet\bullet}$) [25,26]. Disordered structures are electron-trapping or hole-trapping centers and occur by the dislocation of Mg or Ti atoms in the octahedral clusters in the MTO crystal. Effective charge separations (electron–hole) require the presence of cluster-to-cluster charge transfer (CCCT) processes [26] and are strongly dependent on the formation and recombination of all complex clusters present in MTO materials, which are described in the following equations:

$$[TiO_6]^x + [TiO_5 \cdot V_O^x] \rightarrow [TiO_6]' + [TiO_5 \cdot V_O^\bullet] \quad (2)$$

$$[TiO_6]^x + [TiO_5 \cdot V_O^x] \rightarrow [TiO_6]' + [TiO_5 \cdot V_O^{\bullet\bullet}] \quad (3)$$

$$[MgO_6]^x + [MgO_5 \cdot V_O^x] \rightarrow [MgO_6]' + [MgO_5 \cdot V_O^\bullet] \quad (4)$$

$$[MgO_6]^x + [MgO_5 \cdot V_O^x] \rightarrow [MgO_6]' + [MgO_5 \cdot V_O^{\bullet\bullet}] \quad (5)$$

Structural and electronic reconstructions of all possible combinations of clusters belonging to a specific crystal are essential for understanding the PL phenomenon [26]. Previously reported theoretical and experimental studies have shown that defects as the network clusters are formed are responsible for generating deeper defects in the structures of these materials when compared with the same type of defect generated in the network modifier, i.e., the disorder forming network polarizes the structure with greater ease with a base in the local structure [7]. The increase in the treatment temperature of MTO in particular is responsible for promoting the evolution of a crystallization process in these materials, where associated shallow defects are eliminated and the deeper defects remain which can be easily observed in the PL spectra (see Figure 4) and are in good agreement with our XRD and MR results (see Figures 1 and 2).

In particular, the infrared emission is a lower energetic emission and can be related to deeper defects in the band gap region which originate due to the presence of a larger concentration of the $[TiO_5 \cdot V_O^{\bullet\bullet}]$ or $[TiO_5 \cdot V_O^\bullet]$ complex clusters. A decrease in emission intensity is observed in the NIR region (see Figure 4(c, d)) due to the increase of the concentration of Sr-doped MTO where the incorporation of the dopant element is responsible for the structural organization at the short-range and long-range (see Figures 1 and 2). As the crystallization evolves, the atomic crystalline structure renders a better electronic configuration, which increases the PL emission. These results present an important contribution toward a deeper understanding of the impact of the local disorder in perovskite materials, which is responsible for modulating the physical and chemical properties. Two effects in the emission of the MTO samples can be identified. The first effect is intrinsic to perovskite material derived from bulk material that is made up of asymmetric distorted $[MgO_6]$ and $[TiO_6]$ octahedral which allows the excited $[MgO_6]$ and $[TiO_6]$ octahedra groups. This excited state favors the population of intermediary energy levels within the band gap of this material. The second effect is a consequence of the surface and interface complex cluster defect that produce extrinsic defects that also decrease the band gap and allow PL emission. The interplay between the cluster distortions and the surface defects generates a specific PL emission color. Before the photon arrival, the short- and middle-range structural defects generate localized states within the band gap and a non-homogeneous charge distribution in the cell. After the photon arrival, the lattice configuration changes, and distorted excited clusters are formed, allowing electrons to become trapped. In the latter, the photons decay by radiative or non-radiative relaxations.

Based on these findings and from previous research, these ideas can be generalized to other cases, thus expanding the knowledge about the nature of the PL behavior in semiconductor materials based on order-disorder effects at short-, middle- and long-range. Thus, it is shown that locations where the structural defects in the network modifier have a more important and significant role on the PL emission behavior are expected to have a stronger emission in the blue spectral region due to the presence of a higher concentration of the short-range structural defects. In systems where the PL behavior is dominated by long-range defects, that are closely associated with structural defects linked to the disorder forming network a strong emission in the red spectral region is expected. Finally the structural defects in the middle-range can be associated with a balanced contribution of defects in the former and modifier network. This study showed that PL emission is affected by the structural defects in the network former and in the network modifier due to the replacement of Mg^{2+} by Sr^{2+} ions. Therefore, the deviations observed in the spectroscopic properties of these systems can be understood in an intuitive way based on the presence of structural defects at the short-, middle- and long-range, which are associated with the disorder in the former and modifier networks. These ideas lead to new perspectives and provide a solid base that contributes to a deeper understanding of the physical and chemical properties of semiconductor materials beyond those discussed in this letter.

4. Conclusions

In summary, we have reported the synthesis and photoluminescence properties of synthesized MTO and MTO:Sr calcined at various temperatures for 2 h. The quantitative analysis of the results obtained by XRD, MR, FE-SEM, UV–vis, and PL measurements was employed to provide valuable insights into the short-, medium- and long-range structural defect concentrations and allow the proposal of a possible model to explain the PL behavior of the MTO and MTO:Sr samples based on order-disorder effects. Moreover, the results showed that the MTO and MTO:Sr samples treated at 600 and 700 °C were ordered at the short- and long-range, as confirmed by XRD and MR, and were disordered at the medium-range as shown by the PL investigations.

Our results show that samples that were heat treated at 700 °C crystallize in a rhombohedral structure. The PL phenomenon in MTO and MTO:Sr MTO at room temperature is directly influenced

by the structural disorders that yield discrete levels in the forbidden band gap. Our findings explain the shift in PL behavior from blue to NIR emission, which is caused by different concentrations of deep and shallow defects in the samples and enables the design of different colored materials. These results provide useful insights into designing a new series of NIR-emitting materials based on MTO that have a wide range of potential applications. We believe that these materials can be useful for the design of new electro-optic devices.

Acknowledgments

The authors appreciate the support of the Brazilian research financing institutions: CAPES, FAPESP/CEPID 2011/, INCTMN – CNPq (573636/2008-7) FAPESP.

Appendix A. Supplementary data

Supplementary data associated with this article can be found, in the online version, at doi:10.1016/j.cplett.2015.01.011.

References

[1] R.H. Mitchell, Perovskites Modern and Ancient, vol. 57, Almaz Press Inc., Canada, 2002, pp. 317.
[2] P. Gao, M. Grätzel, M.K. Nazeeruddin, Energy Environ. Sci. 7 (2014) 2448.
[3] F. Brivio, A.B. Walker, A. Walsh, Appl. Phys. Lett. Mater. 1 (2013) 04211.
[4] A.E. Nogueira, E. Longo, E.R. Leite, E.R. Camargo, J. Colloid Interface Sci. 415 (2014) 89.
[5] T.M. Mazzo, et al., J. Alloys Compd. 585 (2014) 154.
[6] T. Surendar, S. Kumar, V. Shanker, Phys. Chem. Chem. Phys. 16 (2014) 728.
[7] E.A.V. Ferri, et al., J. Phys. Chem. C 116 (2012) 15557.
[8] F.A. La Porta, J. Andres, M.S. Li, J.R. Sambrano, J.A. Varela, E. Longo, Phys. Chem. Chem. Phys. 16 (2014) 20127.
[9] F.A. La Porta, et al., J. Alloys Compd. 556 (2013) 153.
[10] X. Zhou, Y. Yuan, L. Xiang, Y. Huang, J. Mater. Sci. 42 (2007) 6628.
[11] Q.L. Zhang, H. Yang, J. Mater. Sci. Mater. Electron. 18 (2007) 967.
[12] V.M. Ferreira, J.L. Baptista, J. Petzelt, G.A. Komandin, V.V. Voitsekhovskii, Mater. Res. 10 (1995) 2301.
[13] V.S. Marques, et al., Solid State Sci. 10 (2008) 1056.
[14] Y.-D. Ho, C.-L. Huang, J. Am. Ceram. Soc. 96 (2013) 2065.
[15] E. Korkmaz, N.O. Kalaycioglu, V.E. Kafadar, Bull. Mater. Sci. 36 (2013) 1079.
[16] M.M. Ferrer, Y.V.B. de Santana, C.W. Raubach, F.A. La Porta, A.F. Gouveia, E. Longo, J.R. Sambrano, J. Mol. Model. 20 (2014) 2375.
[17] T.M. Mazzo, et al., Opt. Mater. 32 (2010) 990.
[18] Y.H. Choi, J. Lee, Thin Solid Films 385 (2001) 43.
[19] E.A.V. Ferri, et al., Mater. Chem. Phys. 117 (2009) 192.
[20] G. Carta, R. Gerbasi, G. Rossetto, P. Zanella, M. Natali, M. Bolzan, O. Saoncella, Surf. Coat. Technol. 201 (2007) 9117.
[21] K. Momma, F. Izumi, J. Appl. Crystallogr. 44 (2011) 1272.
[22] T. Hirata, K. Ishioka, M.J. Kitajima, Solid State Chem. 124 (1996) 353.
[23] B. Reynard, F. Guyot, Phys. Chem. Miner. 21 (1994) 441.
[24] C.-H. Wang, X.P. Jing, W. Feng, J. Lu, J. Appl. Phys. 104 (2008) 034112.
[25] E. Longo, et al., Phys. Rev. B 69 (2004) 125115.
[26] V.M. Longo, et al., J. Phys. Chem. C 115 (2011) 5207.
[27] F.A. La Porta, et al., J. Mater. Chem. C 2 (2014) 10164.